

Research Article

Support Vector Machine-Based Backprojection Algorithm for Detection of Gastric Cancer Lesions with Abdominal Endoscope Using Magnetic Resonance Imaging Images

Huajia Dai , Yuhao Bian , Libin Wang , and Junfeng Yang 

Department of General Surgery, Shidong Hospital, Shanghai 200438, China

Correspondence should be addressed to Junfeng Yang; richyjf@usst.edu.cn

Received 14 March 2021; Revised 13 April 2021; Accepted 2 May 2021; Published 8 May 2021

Academic Editor: Gustavo Ramirez

Copyright © 2021 Huajia Dai et al. This is an open access article distributed under the Creative Commons Attribution License, which permits unrestricted use, distribution, and reproduction in any medium, provided the original work is properly cited.

This study was to analyze the diagnostic value of magnetic resonance imaging (MRI) for gastric cancer (GC) lesions and the treatment effect of complete laparoscopic radical resection (CLSRR). A malignant tumor recognition algorithm was constructed in this study based on the backprojection (BP) and support vector machine (SVM), which was named BPS. 78 GC patients were divided into an experimental group (received CLSRR) and a control group (received assisted laparoscopic radical resection (ALSRR)), with 39 cases in each group. It was found that the BPS algorithm showed lower relative mean square error (MSE) in axle x ($O_{MSE, x}$) and axle y ($O_{MSE, y}$), but the classification accuracy (CA) was the opposite ($P < 0.05$). The postoperative hospital stay, analgesia duration, first exhaust time (FET), and first off-bed activity time (FOBA) for patients in the experimental group were less ($P < 0.05$). The operation time of the experimental group (270.56 ± 90.55 min) was significantly longer than that of the control group (228.07 ± 75.26 min) ($P < 0.05$). There were 3 cases of anastomotic fistula, 1 case of acute peritonitis, and 2 cases of lung infections in the experimental group, which were greatly less than those in the control group (7 cases, 4 cases, and 3 cases) ($P < 0.05$). In short, the BPS algorithm was superior in processing MRI images and could improve the diagnostic effect of MRI images. The CLSRR could reduce the length of hospital stay and the probability of complications in GC patients, so it could be used as a surgical plan for the clinical treatment of advanced GC.

1. Introduction

Gastric cancer (GC) is a malignant tumor originating from the epithelium of the gastric mucosa. It ranks the first in the incidence of various malignant tumors in China. With the changes in people's lifestyle and eating habits in recent years, the incidence has also increased year by year. It has become one of the major diseases that threaten people's lives worldwide [1, 2]. Nearly half of early GC patients have no obvious clinical symptoms; only some of them have mild indigestion and other symptoms, such as upper abdominal pain, discomfort, slight fullness, pain, nausea, and belching. In addition, these symptoms are not unique to GC [3, 4]. It is not completely clear what causes GC, but most studies have shown that the cause of GC may be mainly related to *Helicobacter pylori* infection and long-term chronic benign gastric diseases. At present, surgical treatment is still the

basis of GC clinical treatment, and chemotherapy and radiotherapy are all adjuvant treatments [5]. Among them, GC radical resection refers to the complete resection of the cancerous tissues of the stomach and the surrounding tissues that may be involved in the infiltration. It is mainly divided into three types: total gastrectomy, partial gastrectomy of the upper root, and partial gastrectomy of the lower root [6].

Traditional examinations for GC in clinic mainly rely on gastric endoscopy. Unfortunately, although gastroscopy is the currently recognized the gold standard for GC diagnosis, it has a low degree of clarity on gastric mucosal lesions, cannot well evaluate submucosal lesions and tumor infiltration depth, and affects adjacent organ. Thus, more accurate examination methods are urgently needed. Magnetic resonance imaging (MRI), as a relatively new imaging method in imaging technology, is widely used in clinical practice and has also become an important evaluation

method for GC diagnosis and staging [7, 8]. MRI can clearly show the structure of each layer of the stomach and the degree of GC infiltration, which is almost the same as the histological results. It has the advantages of multiparameter, high resolution, and high accuracy. Of course, MRI also has corresponding shortcomings, such as a long scan time, poor scan results for elderly patients, and being prone to artifacts and noise [9, 10]. Backprojection (BP) is an accurate time-domain imaging algorithm, which can be applied to image focusing of echo data under any configuration and nonlinear aperture. It has a better image presentation, but the running time is long. Support vector machine (SVM) is a supervised learning model using classification and regression analysis to analyze data, which can identify the size and shape of tumors [11]. Therefore, it considered combining the SVM and BP algorithm in this study to build a GC tumor detection model.

In summary, the BP algorithm has a wide range of application values in image processing. Based on this, a malignant tumor recognition algorithm named BPS was constructed based on the BP and SVM algorithms, and the traditional BP imaging algorithm and SVM algorithm were introduced for comparative analysis. In addition, the BPS algorithm was applied to MRI diagnosis of 78 GC patients, and the treatment effects of 39 cases in the experimental group and 39 cases in the control group were compared so as to comprehensively evaluate the diagnostic value of MRI for GC lesions and the treatment effect of complete laparoscopic radical resection (CLSRR).

2. Materials and Methods

2.1. Selection of Research Samples. A total of 78 GC patients who were admitted to the hospital from March 20, 2018, to April 15, 2020, were selected as the research objects. According to the different surgical methods selected based on the MRI image diagnosis results, they were divided into an experimental group and a control group, with 39 cases in each group. There were 25 males and 14 females in the experimental group, aged 21–69 years old, and 25 males and 14 females in the control group, aged 18–73 years old. The Tumor Node Metastasis (TNM) Staging System (the eighth edition) established by the American Joint Committee on Cancer (AJCC) and the International Union Against Cancer (UICC) was used to evaluate the T1, T2, T3, and T4 staging of patients with GC. The experiment had been approved by the Medical Ethics Committee of the hospital, and the patients and their families had understood the situation of the experiment and signed the informed consent forms.

The inclusion criteria include patients diagnosed with primary GC by pathology; patients older than 18 years old; patients who had not received relevant chemotherapy or drug treatment before surgery; and patients with clear consciousness.

The exclusion criteria include patients with other malignant tumors; patients with tumor metastasis; patients undergoing palliative surgery; patients who withdrew from the experiment due to their own reasons; and patients requiring open surgery from laparoscopic surgery.

2.2. Treatment Methods

2.2.1. CLSRR. Lymph node dissection, tissue freeing, and digestive tract should be reconstructed under laparoscopy. Firstly, a longitudinal incision of about 3 cm was cut at the umbilicus of the patient, and the excised specimen was taken out; a linear cutting closer was adopted to separate the stomach, duodenum, and other parts; the duodenum and remnant stomach were closed, and the final anastomosis was completed. Next, a linear cutting closer was placed to close the distal jejunum and remnant stomach and close the common opening. Then, a reverse puncture was used to complete the Roux-en-Y anastomosis of the esophagus and jejunum, and the proximal jejunum stump and the distal jejunum were anastomosed side to side about 50 cm from the gastrointestinal anastomosis.

2.2.2. Assisted Laparoscopic Radical Resection (ALSRR). After the lymph node dissection and tissue dissociation were completed under laparoscopy, an incision about 6 cm below the xiphoid process was selected for gastrectomy and the specimen was taken out to complete the gastrointestinal anastomosis.

2.3. MRI. The Magnetom Avanto 3.0 T superconducting high-field MRI scanner produced by Siemens in Germany was adopted to scan the patients. During the scan, the patient was in a supine position with steady breathing. The scan was started from 10 cm from the diaphragm to the lower pole of the kidney. The scanning parameters were defined as follows: the matrix was 356×356 , the layer thickness was 2.5 mm, the layer spacing was 0.25 mm, the field of view was 15×15 cm, the TR was 450 ms, and the TE was 15 ms. After the scan is completed, the images are sent to Siemens Syngo software for image reconstruction and diagnostic analysis, and the thickness of normal and diseased stomach walls is recorded.

2.4. BPS Algorithm Based on BP and SVM. The diagnosis of malignant tumors could be regarded as a binary classification issue, such as treating healthy tissues as a positive category and tumor tissues as a negative category, respectively. SVM was the latest technology applied to classification, and it was the best at handling two classification issues. Therefore, the finite difference time domain (FDTD) was introduced firstly in this study [12] to obtain the simulated radar data, the obtained data were undertaken as the machine learning input data of SVM, and then the output data were the category label (positive or negative). It was assumed that the output label of tumor cells was 1, the output label of normal tissue cells was 0, and the imaging area was divided into multiple grids; then the amplitude value of each grid could be calculated using the BP algorithm. The following equation could be obtained:

$$I(s) = \frac{T(s)}{V}. \quad (1)$$

In equation (1), $T(s)$ represented the actual propagation path of electromagnetic waves, $l(s)$ represented the actual propagation distance of electromagnetic waves, and V referred to the propagation speed of electromagnetic waves. The propagation of electromagnetic waves was impossible to be a straight line due to the existence of various organs and tissues in the human body, so it was assumed that there were multiple media in the human body in this study, which were recorded as air medium a (the relative dielectric constant was θ_1 and the conductivity was κ_1) and organ tissue medium b (the relative dielectric constant was θ_2 and the conductivity was κ_2); then the field distributions in the air medium a could be expressed as follows:

$$E_1 = e_x [E_{p1} e^{-um_1 z} + E_{q1} e^{um_1 z}], \quad (2)$$

$$W_1 = e_y \frac{E_{p1} e^{-um_1 z} + E_{q1} e^{um_1 z}}{\omega_0}. \quad (3)$$

In equations (2) and (3), E_{p1} and E_{q1} represented the amplitude of the incident wave and the reflected wave, respectively, m_1 referred to the air wave number, and ω_0 represented the airwave impedance. $m_1 = r\sqrt{\theta_1\kappa_1}$ and $\omega_0 = \sqrt{\kappa_1/\theta_1}$. In addition, r represented the electromagnetic wave emission frequency. Similarly, the field distributions in the organ tissue medium b could be expressed as follows:

$$E_2 = e_x [E_{p2} e^{-um_2(z-c)} + E_{q2} e^{um_2(z-c)}], \quad (4)$$

$$W_2 = e_y \frac{E_{p2} e^{-um_2 z} + E_{q2} e^{um_2 z}}{\omega_1}. \quad (5)$$

In equations (4) and (5), E_{p2} and E_{q2} represented the amplitude of the incident wave and the reflected wave, respectively, m_2 represented the wavenumber of the organ tissue, and ω_1 represented the wave impedance in the organ tissue. $m_2 = r\sqrt{\theta_2\kappa_2}$ and $\omega_1 = \sqrt{\kappa_2/\theta_2}$. The actual propagation distance of electromagnetic waves in the human body could be calculated according to the above methods:

$$l(s)^* = \frac{T(s)^*}{V^*}. \quad (6)$$

In the above equation (6), $l(s)^*$ represented the actual propagation distance of electromagnetic waves in the human body, $T(s)^*$ indicated the actual propagation path of electromagnetic waves in the human body, and V^* referred to the propagation speed of electromagnetic waves in the human body. Then, the electric field amplitude value of each grid could be calculated with the following equation:

$$e(x, y) = \sum_s e(l(s)^*). \quad (7)$$

In equation (7), $e(x, y)$ represented the electric field amplitude value of each grid, and $e(l(s)^*)$ represented the electric field amplitude value of each receiving antenna. Then, the background subtraction method [13] was adopted to extract the signal of the tumor scatterer. The specific steps are shown in Figure 1. Firstly, a simulation experiment was developed under normal stomach conditions, and all the

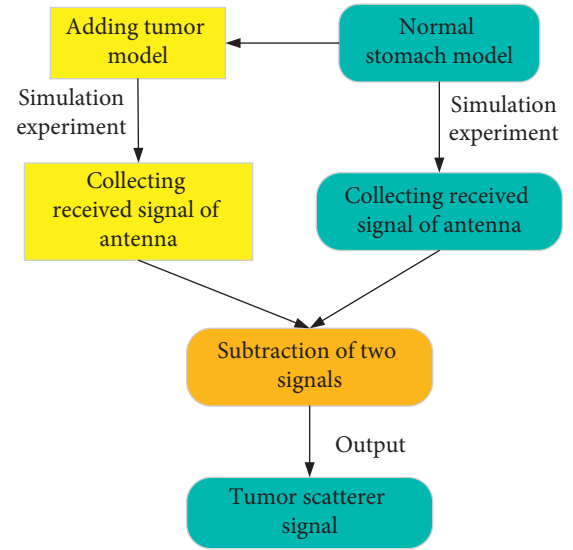


FIGURE 1: Schematic diagram of the signal flow of the background subtraction method to calculate the tumor scatterer.

received signals of the antenna were collected; under the precondition of unchanged parameters, the GC tumor model was added for a simulation experiment again, and all the received signals of the antenna were collected certainly; finally, the received signals of the tumor model were subtracted from the received signals of the normal stomach to obtain the scatterer signals of the tumor.

Then, the obtained tumor scatterer signal was set as E_t , which was undertaken as the input feature vector of SVM learning. The category label of the tumor was supposed as ψ ; then $[E_t, \psi]$ could be considered as a data pair. Some of the data pairs were subjected to the SVM learning, and the category label of each input feature vector was predicted to finally identify the position of the tumor and normal tissue. The malignant tumor recognition algorithm based on BP and SVM was defined as BPS in this study.

2.5. Design of Simulation Experiment. The BRATS2017 public data set was undertaken as the training data. In addition, the traditional BP imaging algorithm [14] and the SVM algorithm [15] were introduced to compare with the BPS algorithm for simulation experiments. The definition position of relative root mean error (RME) and CA of the abscissa and ordinate of the tumor center position were selected as the evaluation indicators of the three algorithms, which were represented with $O_{MES, x}$ and $O_{MES, y}$, respectively, and could be calculated with the following equations:

$$O_{MES, x} = \sqrt{\frac{1}{G} \sum_{i=1}^G \left(\frac{x_{is} - x_{ic}}{h_x} \right)^2}, \quad (8)$$

$$O_{MES, y} = \sqrt{\frac{1}{G} \sum_{i=1}^G \left(\frac{y_{is} - y_{ic}}{h_y} \right)^2}. \quad (9)$$

In equations (8) and (9), $o_{MSE,x}$ and $o_{MSE,y}$ referred to the definition position relative RME of the tumor abscissa and ordinate, respectively; x_{is} and y_{is} indicated the abscissa and ordinate of the actual tumor position, respectively; x_{ic} and y_{ic} referred to the abscissa and ordinate of the predicted tumor position, respectively; h_x and h_y represented the length and the width of the tumor, respectively; and G represented the number of data sets.

2.6. Statistical Methods. The data processing in this study was analyzed by SPSS19.0 version statistical software. The measurement data were expressed as mean \pm standard deviation ($\bar{x} \pm s$), and the count data were indicated as percentage (%). The pairwise comparisons of BP, SBP, and SVM algorithms were realized with the single-factor analysis of variance. The age, body mass index (BMI), tumor size, male-to-female ratio, intraoperative blood loss, number of lymph nodes, operation duration, postoperative hospital stay, analgesia duration, first exhaust time (FET), first off-bed activity time (FOBA), and complications were compared with the paired t test for patients in the two groups. The difference was statistically significant at $P < 0.05$.

3. Results

3.1. Comparison of Diagnosis Performances of Three Algorithms. Figures 2 and 3 are the comparison of $O_{MSE,x}$, $O_{MSE,y}$, and classification accuracy (CA) of the three algorithms. $O_{MSE,x}$, $O_{MSE,y}$, and CA of BP algorithm were 0.31 ± 0.06 , 0.38 ± 0.07 , and 88.41%, respectively; those of the SVM algorithm were 0.35 ± 0.04 , 0.42 ± 0.08 , and 86.65%, respectively; and those of BPS algorithm were 0.14 ± 0.03 , 0.21 ± 0.05 , and 94.56%, respectively. Thus, the BPS algorithm showed dramatic smaller $O_{MSE,x}$ and $O_{MSE,y}$ as well as higher CA in contrast to the BP and SVM algorithms ($P < 0.05$).

3.2. Comparison of Basic Groups of the Two Groups. Figure 4 shows the comparison results of age, BMI, and tumor size of patients in the two groups, and Figure 5 illustrates the comparison results for the ratio of males and females between the two groups. It could be observed that the average age, BMI, tumor size, proportion of males, and proportion of females of patients in the experimental group were 54.61 ± 10.42 years old, $23.51 \pm 4.74 \text{ kg/m}^2$, $4.78 \pm 0.16 \text{ cm}$, 65.34%, and 34.66%, respectively, and those in the control group were 53.78 ± 8.65 years old, $23.89 \pm 5.11 \text{ kg/m}^2$, $4.95 \pm 0.21 \text{ cm}$, 62.85%, and 37.15%, respectively. Thus, the age, BMI, tumor size, ratio of males and females in the experimental group were not obviously different from those in the control group ($P > 0.05$).

3.3. Preoperative MRI Images of Some Patients. Figure 6 shows an MRI image of a male GC patient (46 years old). It showed that the huge cystic solid mass of the abdominal cavity was closely related to the inferior wall of the gastric antrum. The adjacent gastric wall was unevenly thickened. The solid part of the tumor was mainly distributed in the periphery. The solid part of the enhanced arterial phase was

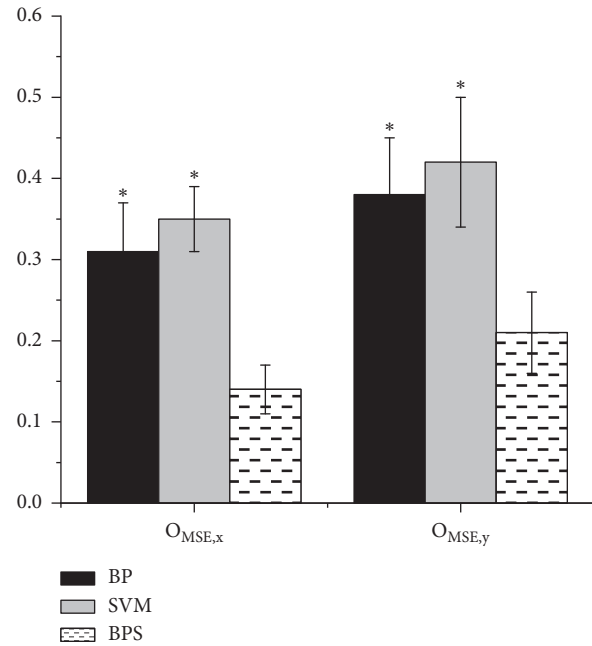


FIGURE 2: Comparison of $O_{MSE,x}$ and $O_{MSE,y}$ of three algorithms.*Statistical difference in contrast to BPS algorithm ($P < 0.05$).

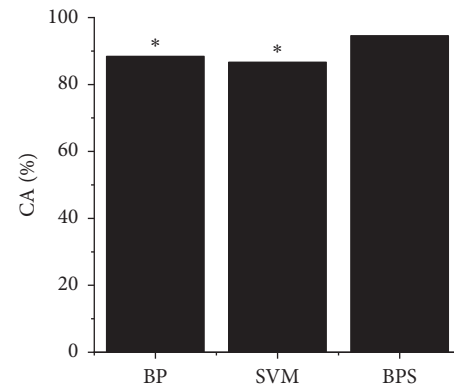


FIGURE 3: Comparison of classification accuracy (CA) of three algorithms.*Statistical difference in contrast to BPS algorithm ($P < 0.05$).

significantly enhanced with a small number of small air bubbles. There were multiple enlarged and ring-shaped enhanced lymph nodes in the arteries. Thus, it could be interpreted as poorly differentiated adenocarcinoma of the stomach. Figure 7 shows an MRI image of a female GC patient (55 years old). It is suggested that the stomach wall was thickened, the submucosal signals were visible, the cancer tumor involved more than half of the thickness of the stomach wall, the signals were uniform throughout the layer, and the serosal surface was smooth. Thus, it could be interpreted as the GC T3 stage.

3.4. Comparison of the Thickness of the Stomach Wall in the Diseased Area and the Normal Area. The thicknesses of the stomach wall in the diseased area and the normal area were

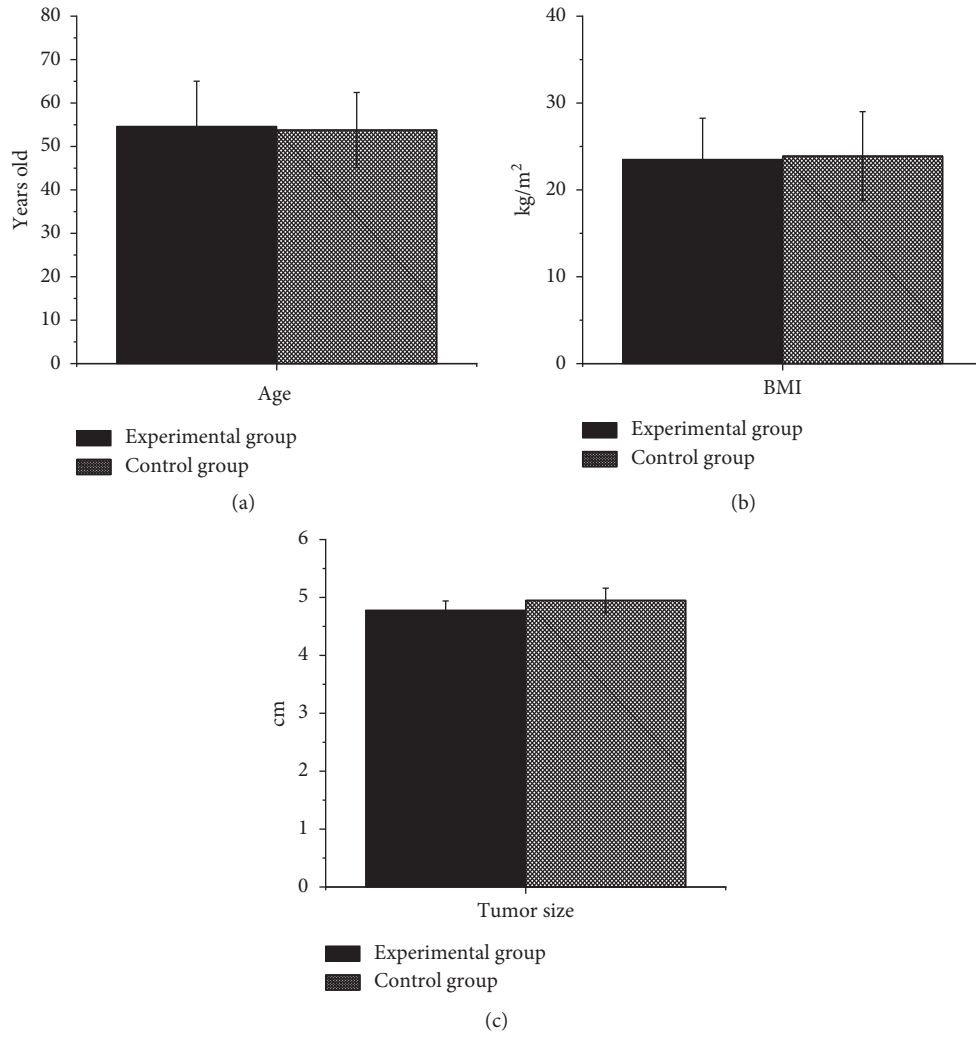


FIGURE 4: Comparison of age, BMI, and tumor size of patients in the two groups. (a, b, c) Comparison of age, BMI, and tumor size, respectively.

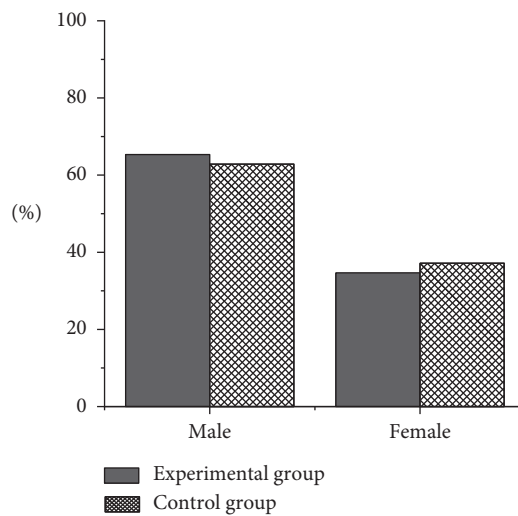


FIGURE 5: The comparison results for the ratio of males and females between the two groups.

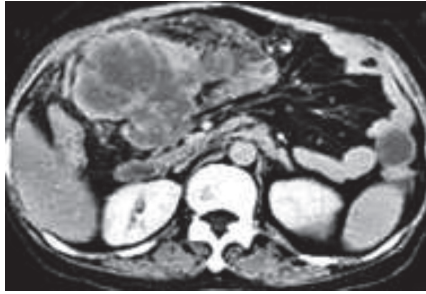


FIGURE 6: A MRI image of a male GC patient (46 years old).

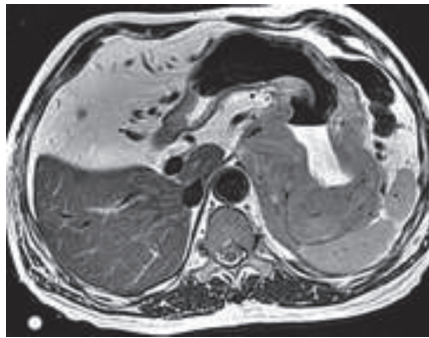


FIGURE 7: A MRI image of a female GC patient (55 years old).

compared, as shown in Figure 8. It suggested that the thickness of the normal stomach wall was 4.52 ± 1.05 mm, while the thicknesses of the stomach walls with GC T1, T2, T3, and T4 stage were 10.88 ± 1.53 mm, 12.17 ± 2.56 mm, 19.45 ± 4.78 mm, and 21.06 ± 3.71 mm, respectively. Thus, it could be concluded that the thickness of the normal stomach wall was observably smaller than that of the GC T1, T2, T3, and T4 stages with a huge difference ($P < 0.05$); the thickness of the stomach wall in the GC T4 stage was much smaller than that of the T1 and T2 stages with a notable difference ($P < 0.05$); the difference in thickness of stomach wall between GC T1 and T2 stages was not obvious enough ($P > 0.05$); and there was no considerable difference in thickness of stomach wall between GC T3 and T4 stage ($P > 0.05$).

3.5. Comparative Analysis of MRI Examination and Pathological Diagnosis Results. Figure 9 shows the comparison between MRI and pathological diagnosis results. It indicated that the diagnostic accuracies of MRI for GC T1, T2, T3, and T4 stage were 80.55%, 76.15%, 96.44%, and 62.45%, respectively. Among them, MRI showed the highest diagnostic accuracy for GC T3 stage and the lowest diagnostic accuracy for GC T4 stage.

3.6. Analysis on Treatment Effect of Radical Resection of the Two Groups of Patients. The intraoperative conditions between the two groups of patients were analyzed and compared, and the results are illustrated in Figure 10. It disclosed that the intraoperative blood loss (239.46 ± 69.44 mL) and the number of lymph nodes (35.28 ± 10.11) in the

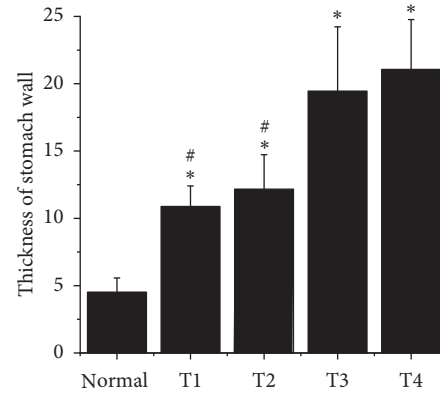


FIGURE 8: The thicknesses of the stomach walls in the diseased area and the normal area. * and # indicated that the difference was great in contrast to the thickness of the normal stomach wall and the thickness of the stomach wall in GC T4, respectively.

experimental group were not greatly different from those in the control group (225.15 ± 80.74 mL and 33.97 ± 8.57) ($P > 0.05$), while the operation duration of the experimental group (270.56 ± 90.55 minutes) was much longer in contrast to that of the control group (228.07 ± 75.26 minutes) ($P < 0.05$).

Figure 11 illustrates a comparison of the postoperative situations of the two groups of patients. It was clear that the postoperative hospital stay, analgesia duration, FET, and FOBA of the experimental group were 6.54 ± 1.53 days, 15.56 ± 1.53 hours, 3.16 ± 0.54 days, and 1.82 ± 0.83 days, respectively, while those in the control group were 8.94 ± 2.02 days, 25.03 ± 5.11 hours, 5.28 ± 1.11 days, and 3.51 ± 0.74 days, respectively. Thus, the postoperative hospital stay, anchorage duration, FET, and FOBA of the experimental group were all greatly lower than those of the control group ($P < 0.05$).

Figure 12 illustrates the comparison of postoperative complications between the two groups of patients. It disclosed that there were 3 cases of postoperative anastomotic leakage, 1 case of acute peritonitis, 2 cases of lung infection, and 2 cases of acute pulmonary embolism in the experimental group, while there were 7 cases of postoperative anastomotic leakage, 4 cases of acute peritonitis, 3 cases of lung infection, and 2 cases of acute pulmonary embolism in the control group. Thus, it was clear that the numbers of cases with anastomotic leakage, acute peritonitis, and lung infection in the experimental group were much less ($P < 0.05$), while the number of cases with acute pulmonary embolism in the two groups was not extremely different ($P > 0.05$).

4. Discussion

LRSR is a widely accepted treatment for GC in clinic, but most of them are ALRSRs. The high-tech laparoscopic gastrointestinal reconstruction is still in the preliminary application stage. MRI can further show the GC lesions, but the quality of the original image is affected by various objective factors [16]. Therefore, the BPS algorithm was

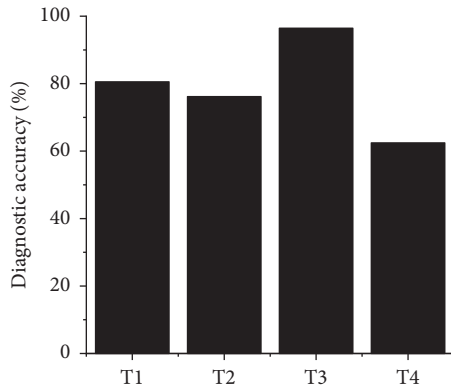


FIGURE 9: The comparison between MRI and pathological diagnosis results.

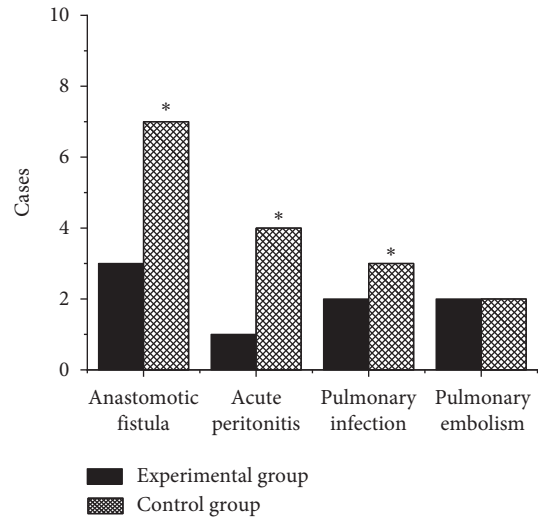


FIGURE 12: The comparison of postoperative complications between the two groups of patients. *Extreme difference in contrast to the experimental group ($P < 0.05$).

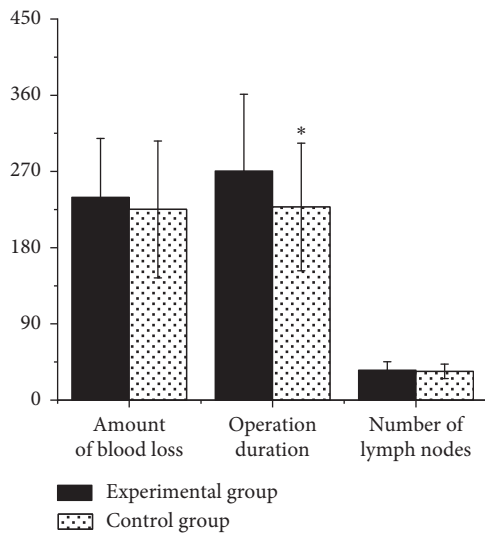


FIGURE 10: The intraoperative conditions between the two groups of patients. *Dramatic difference in contrast to the experimental group ($P < 0.05$).

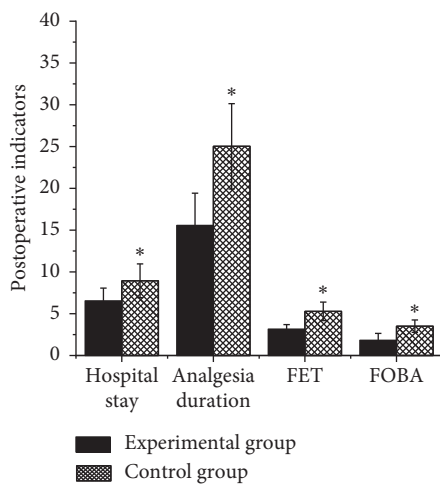


FIGURE 11: A comparison of the postoperative situations of the two groups of patients. *The difference was great in contrast to the experimental group ($P < 0.05$).

constructed based on BP and SVM in this study, and the traditional BP imaging algorithm and SVM algorithm were introduced for comparative analysis. It was found that the BPS algorithm showed visible smaller $O_{MSE, x}$ and $O_{MSE, y}$ as well as higher CA than the BP and SVM algorithms ($P < 0.05$), which was similar to the results of Hu et al. [17]. It indicated that the BPS algorithm constructed in MRI could show excellent performance in image processing and could improve the diagnostic effect of MRI images. The BPS algorithm was applied to 78 cases of GC patients for MRI diagnosis, and the results found that the diagnostic accuracies of MRI for GC T1, T2, T3, and T4 stage were 80.55%, 76.15%, 96.44%, and 62.45%, respectively. Such results were consistent with the conclusion of Hu et al. [18], revealing that MRI images based on the BPS algorithm had a good diagnostic effect for GC staging.

Then, the treatment effects of 39 cases in the experimental group and 39 cases in the control group were compared comprehensively. The results showed that the intraoperative blood loss (239.46 ± 69.44 mL) and the number of lymph nodes (35.28 ± 10.11 mL) in the experimental group were not greatly different from those in the control group (225.15 ± 80.74 mL and 33.97 ± 8.57 mL) ($P > 0.05$), while the operation duration (270.56 ± 90.55 minutes) was longer in the experimental group in contrast to the control group (228.07 ± 75.26 minutes) ($P < 0.05$). It was different from the conclusion of Li et al. [19], which may be due to the complete technical requirements of the surgery. Such results showed that the operation duration of CLSRR was longer, but the effect on intraoperative bleeding was not obvious. The postoperative hospital stay, analgesia duration, FET, and FOBA of patients in the experimental group were all shorter observably ($P < 0.05$), indicating that the CLSRR showed a better treatment effect for patients regardless of the longer operation duration [20]. The numbers of cases suffered from postoperative anastomotic leakage, acute peritonitis, and lung infection in the experimental group were much less

($P < 0.05$), indicating that the CLSRR could reduce the risk of postoperative complications in GC patients.

5. Conclusion

A BPS algorithm was constructed based on BP and SVM algorithms firstly, and then these three algorithms were compared for deep analysis. In addition, the BPS algorithm was applied to 78 GC patients for MRI diagnosis. The treatment of 39 cases in the experimental group and 39 cases in the control group was compared. It was found that the BPS algorithm constructed showed excellent performance in MRI image processing and could improve the diagnostic effect of MRI images. Compared with the ALSRR, the CLSRR could reduce the hospital stay and complications of GC patients after surgery and could be used as a clinical treatment for advanced GC. However, there were still some shortcomings in this study. The sample size of the selected patients was small, and long-term follow-up records were not carried out. There was a lack of long-term data on patient rehabilitation. Therefore, in the follow-up, it will consider increasing the selection of patient samples, conducting long-term follow-up, and discussing the prognostic effect of CLSRR. In short, the results of this study provided a theoretical basis for the clinical diagnosis and treatment of GC.

Data Availability

No data were used to support this study.

Conflicts of Interest

The authors declare that they have no conflicts of interest.

References

- [1] K. Buder-Bakhaya and J. C. Hassel, "Biomarkers for clinical benefit of immune checkpoint inhibitor treatment—a review from the melanoma perspective and beyond," *Frontiers in Immunology*, vol. 9, p. 1474, 2018.
- [2] S.-E. Al-Batran, N. Homann, C. Pauligk et al., "Effect of neoadjuvant chemotherapy followed by surgical resection on survival in patients with limited metastatic gastric or gastroesophageal junction cancer," *JAMA Oncology*, vol. 3, no. 9, pp. 1237–1244, 2017.
- [3] M. Coskun, "Hepatocellular carcinoma in the cirrhotic liver: evaluation using computed tomography and magnetic resonance imaging," *Experimental and Clinical Transplantation: Official Journal of the Middle East Society for Organ Transplantation*, vol. 15, no. S2, pp. 36–44, 2017.
- [4] J. Chen, R. Zhang, C. Tao et al., "CuS-NiS₂ nanomaterials for MRI guided phototherapy of gastric carcinoma via triggering mitochondria-mediated apoptosis and MLKL/CAPG-mediated necroptosis," *Nanotoxicology*, vol. 14, no. 6, pp. 774–787, 2020.
- [5] L. Ma, X. Xu, M. Zhang et al., "Dynamic contrast-enhanced MRI of gastric cancer: correlations of the pharmacokinetic parameters with histological type, Lauren classification, and angiogenesis," *Magnetic Resonance Imaging*, vol. 37, pp. 27–32, 2017.
- [6] G. Zheng, X. Cheng, L. Wang et al., "Correlation of MRI apparent diffusion coefficient with molecular marker Ki-67 in gastric cancer," *Zhonghua Wei Chang Wai Ke Za Zhi*, vol. 20, no. 7, pp. 803–808, 2017.
- [7] K. Haruki, T. Misawa, T. Gocho et al., "Hepatocellular carcinoma with gastric metastasis treated by simultaneous hepatic and gastric resection: report of a case," *Journal of Clinical Gastroenterology*, vol. 9, no. 5, pp. 319–323, 2016.
- [8] D. H. Lee, S. H. Kim, I. Joo, B. Y. Hur, and J. K. Han, "Comparison between 18F-FDG PET/MRI and MDCT for the assessment of preoperative staging and resectability of gastric cancer," *European Journal of Radiology*, vol. 85, no. 6, pp. 1085–1091, 2016.
- [9] X. Ji, F. Chen, Y. Zhou et al., "Copy number variation profile in noninvasive prenatal testing (NIPT) can identify co-existing maternal malignancies: case reports and a literature review," *Taiwanese Journal of Obstetrics and Gynecology*, vol. 57, no. 6, pp. 871–877, 2018.
- [10] A. S. Borggreve, S. E. Heethuis, M. R. Boekhoff et al., "Optimal timing for prediction of pathologic complete response to neoadjuvant chemoradiotherapy with diffusion-weighted MRI in patients with esophageal cancer," *European Radiology*, vol. 30, no. 4, pp. 1896–1907, 2020.
- [11] J. Li, P. Liang, D. Zhang et al., "Primary carcinosarcoma of the liver: imaging features and clinical findings in six cases and a review of the literature," *Cancer Imaging*, vol. 18, no. 1, p. 7, 2018.
- [12] E. G. Klompenhouwer, R. C. Dresen, C. Verslype et al., "Safety and efficacy of transarterial radioembolisation in patients with intermediate or advanced stage hepatocellular carcinoma refractory to chemoembolisation," *Cardiovascular and Interventional Radiology*, vol. 40, no. 12, pp. 1882–1890, 2017.
- [13] A. K. K. Minn, N. Sato, M. N. Mieno, T. Arai, and M. Muramatsu, "Association study of long non-coding RNA HOTAIR rs920778 polymorphism with the risk of cancer in an elderly Japanese population," *Gene*, vol. 729, Article ID 144263, 2020.
- [14] Z. Lin, J. Chen, and Y. Guo, "Efficacy of XELOX adjuvant chemotherapy for gastric mixed adenoneuroendocrine carcinoma: a case report," *Medicine (Baltimore)*, vol. 98, no. 23, Article ID e16000, 2019.
- [15] Y. Zhao, J. Y. He, Y. L. Zou et al., "Evaluating the cerebrospinal fluid ctDNA detection by next-generation sequencing in the diagnosis of meningeal carcinomatosis," *BMC Neurology*, vol. 19, no. 1, p. 331, 2019.
- [16] J. Chen, G. Ren, R. Cai et al., "Cellular magnetic resonance imaging: in vivo tracking of gastric cancer cells and detecting of lymph node metastases using microparticles of iron oxide in mice," *Cancer Management and Research*, vol. 11, pp. 7317–7326, 2019.
- [17] J. Hu, W. Zhang, and X. Chen, "[Laparoscopic gastrectomy combined with neoadjuvant chemotherapy for gastric cancer patients: from the view of the CLASS-03a trial]," *Zhonghua Wei Chang Wai Ke Za Zhi*, vol. 21, no. 2, pp. 138–142, 2018.
- [18] Y. Hu, C. Huang, Y. Sun et al., "Morbidity and mortality of laparoscopic versus open D2 distal gastrectomy for advanced gastric cancer: a randomized controlled trial," *Journal of Clinical Oncology*, vol. 34, no. 12, pp. 1350–1357, 2016.
- [19] H.-Z. Li, J.-X. Chen, Y. Zheng, and X.-N. Zhu, "Laparoscopic-assisted versus open radical gastrectomy for resectable gastric cancer: systematic review, meta-analysis, and trial sequential analysis of randomized controlled trials," *Journal of Surgical Oncology*, vol. 113, no. 7, pp. 756–767, 2016.
- [20] A. Neyaz, N. Husain, M. Deodhar, R. Khurana, S. Shukla, and A. Arora, "Synchronous cervical minimal deviation adenocarcinoma, gastric type adenocarcinoma and lobular endocervical glandular hyperplasia along with STIL in peutz-jeghers syndrome: eliciting oncogenesis pathways," *Türk Patoloji Dergisi*, vol. 35, no. 3, pp. 247–253, 2019.